

ELECTRONIC SUPPLEMENTARY INFORMATION

Effect of molecular geometry and extended conjugation on the performance of hydrogen-bonded semiconductors in organic thin-film field-effect transistors

Paula Gómez,^{†a} Jesús Cerdá,^{†b} Miriam Más-Montoya,^a Stamatis Georgakopoulos,^a Iván da Silva,^c Antonio García,^a Enrique Ortí,^{*b} Juan Aragón^{*b} and David Curiel^{*a}

^a Multifunctional Molecular Materials Group, Department of Organic Chemistry, University of Murcia, Campus of Espinardo, 30100-Murcia, Spain. E-mail: davidcc@um.es

^b Instituto de Ciencia Molecular, Universidad de Valencia, Catedrático José Beltrán 2, 46980 Paterna, Spain. E-mail: enrique.orti@uv.es, juan.arago@uv.es

^c ISIS Facility, STFC Rutherford Appleton Laboratory, Chilton, Oxfordshire OX11 0QX, UK

[†] P.G. and J.C. contributed equally to this work.

Content

General.....	S2
OFETs fabrication and characterisation.....	S2
Atomic Force Microscopy.....	S2
X-ray diffraction.....	S3
Computational methods.....	S3
Synthetic procedures.....	S4
NMR spectra.....	S6
Thermal characterisation.....	S8
Molecular orbitals.....	S9
TD-DFT calculations.....	S9
Thin-film OFET characteristics.....	S10
X-ray diffraction data and molecular packing.....	S10
Atom-to-atom non-covalent interactions.....	S12
2D maps of transfer integrals in π -stacked dimers.....	S13
MD simulation of transfer integrals in π -stacked dimers.....	S14
References.....	S15

EXPERIMENTAL SECTION

General

Solvents and chemical reagents were purchased from commercial sources and were used as received. The final products were purified by train sublimation (pressure < 10⁻⁶ mbar). Melting points were measured in a Reichert instrument and were not corrected. Thermogravimetric analyses (TGA) were done in a SDT 2960 analyzer from TA Instruments working under inert atmosphere at a heating rate of 10 °C min⁻¹. Differential scanning calorimetry (DSC) was performed in a DSC 822E Mettler Toledo equipment with a 50 mL min⁻¹ nitrogen flow and a heating rate of 10 °C min⁻¹. Bruker AV300, Bruker AV400, or Bruker AV600 NMR spectrometers were used for the acquisition of ¹H-NMR and ¹³C-NMR spectra. The chemical shifts were referenced to the residual peaks of the deuterated solvents. Mass spectra were measured on an HPLC-MS TOF 6220 instrument. Absorption spectra were acquired on a Cary 5000 spectrophotometer using DMF solutions (2.5 × 10⁻⁵ M). Solid-thin films for UV-vis measurements were prepared by thermal evaporation on quartz substrates. Cyclic voltammetry experiments were performed using a BAS potentiostat in dimethylformamide (DMF) solution with tetrabutylammonium hexafluorophosphate (0.1 M) as supporting electrolyte and at a scan rate of 100 mV s⁻¹ (working electrode: boron-doped diamond; reference electrode: Ag/AgCl; counter electrode: Pt wire; internal reference: ferrocene/ferrocenium).

OFETs fabrication and characterisation

P-doped n⁺⁺ silicon wafers coated with a 300 nm-thick layer of thermally grown SiO₂ were used for the fabrication of thin-film OFETs. These substrates were cleaned by sequential sonication in water, acetone and isopropanol for 20 min. Thin-film transistors with a bottom-gate top-contact configuration were fabricated by initially covering the substrate with a polystyrene layer (PS, MW = 3350), deposited by spin-coating (3000 rpm, 30 s) from a toluene solution (1% wt). Then, thin films of organic semiconductors (**BDAI**, **NDAI**, **ADAI** and **PDAI**) were thermally evaporated under high vacuum (1 × 10⁻⁷ mbar) at a rate of 0.1–0.3 Å s⁻¹, until a thickness of 50 nm was reached. Finally, thin-film transistors were completed by the sequential evaporation of 8 nm of MoO₃ (rate: 0.1 Å s⁻¹) and 25 nm of Au (rate: 0.2 Å s⁻¹) through a shadow mask. The OFET channels dimensions were: *W* = 2 mm and *L* = 40–140 μm. The electrical characterisation was performed at room temperature under ambient conditions by measuring the characteristic current–voltage curves (output characteristics: drain current (*I_D*) vs drain voltage (*V_D*); transfer characteristics: drain current (*I_D*) vs gate voltage (*V_G*)), using a Keithley 2636A Source Measure Unit. The field-effect mobilities were extracted in the saturation regime (Eq. S1):

$$\mu = \left(\frac{d\sqrt{I_D}}{dV_G} \right)^2 \frac{2L}{WC_i} \quad \text{Eq. S1}$$

where μ is the field-effect mobility, I_D is the drain current, V_G is the source-gate voltage, L is the channel length, W is the channel width, and C_i is the gate capacitance per unit area.

Atomic Force Microscopy

NT-MDT atomic force microscope (NTEGRA PRIMA), working under tapping mode conditions, was used to obtain AFM images. These were analysed with Gwyddion V2.47.

X-ray diffraction

Powder X-ray diffraction: High-resolution powder X-ray diffraction patterns were measured at the ESRF synchrotron (Grenoble, France) using the Spanish beamline SpLine (BM25A) with a 0.77449 and 0.56523 Å wavelength for **NDAI** and **PDAI**, respectively, at room temperature. Samples were loaded in borosilicate capillary tubes and mounted on a rotatory goniometric head, to reduce the effect of possible preferential orientations. Measurements were performed in a 2θ continuous scan mode, with a 0.004° effective step. The incident beam (dimensions: 10 mm horizontal x 0.5 mm vertical) was monitored to normalize the collected data considering the primary beam decay. The diffracted beam was collected using a point detector. Data were measured within a $3\text{--}32^\circ$ and $3\text{--}40^\circ$ 2θ range for **NDAI** and **PDAI**, respectively, corresponding to an approximate resolution of 1 Å for both cases. The structures of compounds **NDAI** and **PDAI** were solved *ab initio* and refined using Rietveld method with Topas Academic 5 program (<http://www.topas-academic.net/>). Final Rietveld plots are given in Fig. S8, whereas crystallographic and refinement parameters are summarized in Table S2. CCDC 2069806 (**NDAI**) and 2069805 (**PDAI**) contain the supplementary crystallographic data for this paper. Crystal structures of **BDAI** and **ADAI**, 1557392 and 1957368 respectively, have been previously reported. These data can be obtained free of charge from The Cambridge Crystallographic Data Centre (CCDC) via www.ccdc.cam.ac.uk/structures.

Thin film X-ray Diffraction: Data were collected on a Bruker D8 Advance instrument in $\theta\text{--}\theta$ mode with $\text{CuK}\alpha$ radiation (wavelength 1.54060 Å), 40 kV, 30 mA, and a 1-dimensional detector with a window of 1° . Primary optics consisted of a 2° Soller slit, a 1 mm incidence slit and an air scatter screen. Secondary optics included a 3 mm antiscatter slit, a Ni filter and a 2.5° Soller slit. Samples were step scanned from 3 to 65° in 2θ , with 0.05° stepping intervals, 0.1 s per step, and a rotation speed of 30 rpm.

Computational methods

The theoretical characterisation of the **BDAI**, **NDAI**, **ADAI** and **PDAI** compounds was carried out at the B3LYP/6-31G** level,¹⁻³ including the dispersion effects with the Grimme's D3 correction⁴ and the Becke–Johnson dumping function (-D3BJ)^{5,6} as implemented in the Gaussian16 software package in its A03 revision.⁷ Solvent effects (in DMF) were taken into account within the polarizable continuum model (PCM).⁸ The molecular geometries of the molecules investigated were fully optimized without symmetry restrictions and the calculated minimum-energy geometries present minimum deviations from the C_{2h} -symmetry point group. Molecular orbital energies and topologies were computed on these minimum-energy geometries and were plotted by using the Chemcraft 1.8 software.⁹ The lowest-energy singlet-excited states were calculated at the B3LYP/6-31G** level in DMF using the time-dependent density functional theory (TD-DFT) approach.^{10,11}

Hole-transfer integrals $t_{a,b}$ (also known as electronic couplings) were computed by employing the projected method proposed by Baumeirer *et al.*¹² and using the data obtained from B3LYP/6-31G** calculations. In the projection method, the dimer molecular orbitals are projected into the basis of the isolated-molecule molecular orbitals. Fig. S11 displays 2D maps showing the variation of the transfer integral of the face-to-face π -stacked dimers calculated by moving one of the molecules along the x and z directions starting from the crystal structure. To compute the electronic coupling fluctuations due to the thermal motion and, thereby, the effect of the dynamic disorder on the charge transfer integrals, constrained molecular dynamics (MD) simulations were performed at the GFN-FF level.¹³ The constrained MD simulation was carried out for a $5 \times 5 \times 5$ crystal slab (see Fig. S12), where the external

98 molecules were kept frozen. After a 10 ps equilibration step, a 100 ps production MD simulation was conducted and the geometry of the central stacked dimer was extracted each 0.1 ps along the production stage, taking a total of 1000 dimer geometry snapshots. On each snapshot, the electronic coupling was computed and the histogram was fitted to a normal distribution (Fig. S12). The average value and the standard distribution obtained for the transfer integrals are tabulated in Table S3.

The reorganisation energy λ was estimated by using the four-point approach,¹⁴ where the energy difference due to the structural relaxation of the neutral and charged species is computed. Finally, the hole-transfer rate constants (k) were computed according to a Marcus-like expression (Eq. S2). In this expression, $\langle t_{a,b}^2 \rangle$ is the average squared transfer integral between molecular sites a and b , which is computed as $\langle t_{a,b}^2 \rangle = \langle t_{a,b} \rangle^2 + \sigma_t^2$, where $\langle t_{a,b} \rangle$ and σ_t are the average transfer integral and its standard deviation (fluctuation), respectively. λ is the reorganisation energy (only intramolecular in this work), T is the temperature (298.15 K) and $\Delta E_{a,b}$ is the energy difference between the initial and final states that is set to 0.0 eV since both states are energetically equivalent. The values of λ , $\langle t_{a,b}^2 \rangle$ and k are included in Table S3 and are briefly discussed.

$$k = \frac{2\pi}{\hbar} \langle t_{a,b}^2 \rangle \frac{1}{\sqrt{4\pi\lambda k_B T}} \exp\left[-\frac{(\Delta E_{a,b} + \lambda)^2}{4\lambda k_B T}\right] \quad \text{Eq. S2}$$

General procedure for the Buchwald-Hartwig reaction

A mixture of the corresponding aromatic diamine (3.16 mmol), 2,3-dichloropyridine (1.07 g, 7.13 mmol), potassium *tert*-butoxide (1.06 g, 9.48 mmol) and distilled dioxane (20 mL) was prepared in a two-necked round-bottom flask under nitrogen atmosphere. Another two-necked round-bottom flask was charged with (\pm)-2,2'-bis(diphenylphosphino)-1,1'-binaphthalene ((\pm)BINAP) (0.15 g, 7.5 mol%) and distilled dioxane (20 mL) under nitrogen atmosphere. The mixture was heated at 100 °C until a colorless solution was obtained. Afterwards, palladium(II) acetate (Pd(OAc)₂) (0.04 g, 5.0 mol%) was added and the resulting reddish solution was stirred for 15 minutes. The latter solution was added to the first flask via syringe and the mixture was stirred at reflux temperature. The progress of the reaction was checked by thin-layer chromatography employing ethyl acetate:hexane 1:2 as eluent. Once the reaction had been completed, it was cooled down to room temperature and the solvent was removed under reduced pressure. The crude was washed with water (3 × 30 mL) and triturated with methanol (3 × 30 mL) to obtain the desired compound.

General procedure for the photochemical intramolecular coupling reaction

In a photochemical reactor under continuous nitrogen flow, anhydrous dimethyl sulfoxide (160 mL), potassium *tert*-butoxide (0.99 g, 8.84 mmol) and the corresponding *N,N'*-bis(3-chloropyridin-2-yl) aromatic diamine (2.2 mmol) were added. Then, the mixture was degassed for 15 minutes. Afterwards, the reaction was irradiated with a medium-pressure mercury lamp for 2.5 hours. Hereafter, the crude was poured into a cold saturated solution of ammonium chloride and the resulting precipitate was collected by filtration, washed with water (3 × 30 mL) and methanol (3 × 30 mL) to isolate the pure product.

***N,N'*-Bis(3-chloropyridin-2-yl)naphthalene-1,5-diamine, 2.**

Yield: 72%. M.p.: 212 °C. ¹H-NMR (300 MHz, CDCl₃), δ (ppm): 8.13 (d, *J* = 7.5 Hz, 2H), 8.09 (dd, *J* = 4.8, 1.7 Hz, 2H), 7.83 (d, *J* = 8.6 Hz, 2H), 7.64 (dd, *J* = 7.8, 1.7 Hz, 2H), 7.55 (dd, *J* = 8.6, 7.5 Hz, 2H), 7.39 (s, 2H), 6.73 (dd, *J* = 4.8, 7.8 Hz, 2H). ¹³C-NMR (75.5 MHz, CDCl₃), δ (ppm): 152.1, 146.0, 136.7, 135.3, 128.7, 126.0, 119.3, 117.3, 116.4, 115.2. HRMS (ESI) *m/z*: [M+H]⁺ Calcd. for C₂₀H₁₅Cl₂N₄: 381.0668; Found: 381.0665.

7,14-Dihydronaphtho[1,2-*b*:5,6-*b'*]di(7-azaindole), NDAI.

Yield: 65%. M.p.: > 300 °C. ¹H-NMR (300 MHz, DMSO-*d*₆), δ (ppm): 12.79 (s, 2H), 8.60 (dd, *J* = 7.5, 1.8 Hz, 2H), 8.47 (dd, *J* = 4.8, 1.8 Hz, 2H), 8.43 (d, *J* = 8.6 Hz, 2H), 8.38 (d, *J* = 8.6 Hz, 2H), 7.30 (dd, *J* = 7.5, 4.8 Hz, 2H). ¹³C-NMR (75.5 MHz, DMSO-*d*₆), δ (ppm): 151.3, 145.4, 135.7, 128.1, 119.5, 119.4, 116.0, 115.7, 115.6, 114.5. HRMS (ESI) *m/z*: [M+H]⁺ Calcd. for C₂₀H₁₃N₄: 309.1135; Found: 309.1127.

***N,N'*-Bis(3-chloropyridin-2-yl)pyrene-1,6-diamine, 4.**

Yield: 62%. M.p.: 238-240 °C. ¹H-NMR (400 MHz, CDCl₃), δ (ppm): 8.52 (d, *J* = 8.4 Hz, 2H), 8.17 (d, *J* = 8.4 Hz, 2H), 8.13 (d, *J* = 9.2 Hz, 2H), 8.09 (dd, *J* = 4.8, 1.6 Hz, 2H), 8.06 (d, *J* = 9.2 Hz, 2H), 7.68 (dd, *J* = 7.8, 1.6 Hz, 2H), 7.57 (s, 2H), 6.76 (dd, *J* = 7.8, 4.8 Hz, 2H). ¹³C-NMR (101 MHz, CDCl₃), δ (ppm): 152.2, 146.1, 136.8, 132.9, 128.4, 127.7, 125.8, 125.0, 124.5, 122.0, 119.6, 116.4, 115.3. HRMS (ESI) *m/z*: [M+H]⁺ Calcd. for C₂₆H₁₇Cl₂N₄: 455.0825; Found: 455.0807.

5,13-Dihydropyreno[1,2-*b*:6,7-*b'*]di(7-azaindole), PDAI.

Yield: 79%. M.p.: > 300 °C. ¹H-NMR (600 MHz, DMSO-*d*₆), δ (ppm): 12.94 (s, 2H), 9.07 (s, 2H), 8.84 (dd, *J* = 7.8, 1.8 Hz, 2H), 8.72 (d, *J* = 9.0 Hz, 2H), 8.60 (d, *J* = 4.8, 1.8 Hz, 2H), 8.40 (d, *J* = 9.0 Hz, 2H), 7.40 (dd, *J* = 7.8, 4.8 Hz, 2H). ¹³C-NMR could not be measured due to the low solubility of the sample. HRMS (ESI) *m/z*: [M+H]⁺ Calcd. for C₂₆H₁₅N₄: 383.1291; Found: 383.1296.

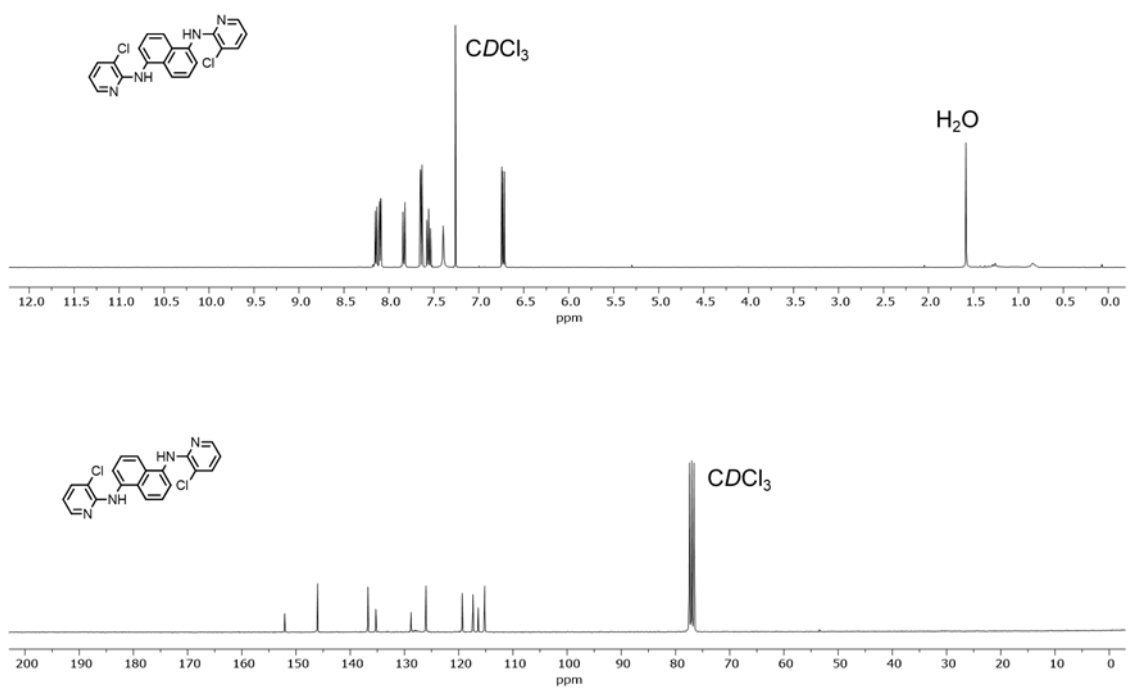


Fig. S1 $^1\text{H-NMR}$ and $^{13}\text{C-NMR}$ spectra of compound **2** in CDCl_3 .

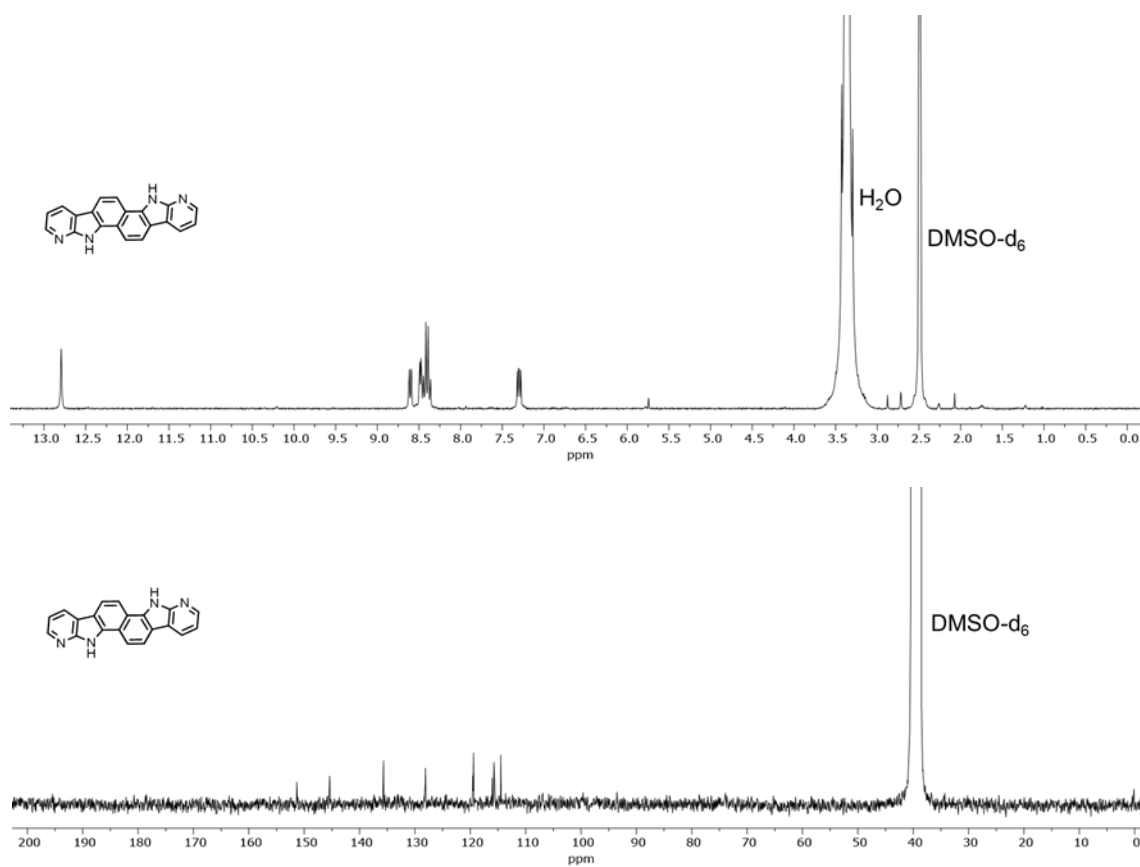


Fig. S2 $^1\text{H-NMR}$ and $^{13}\text{C-NMR}$ spectra of **NDAI** in DMSO-d_6 .

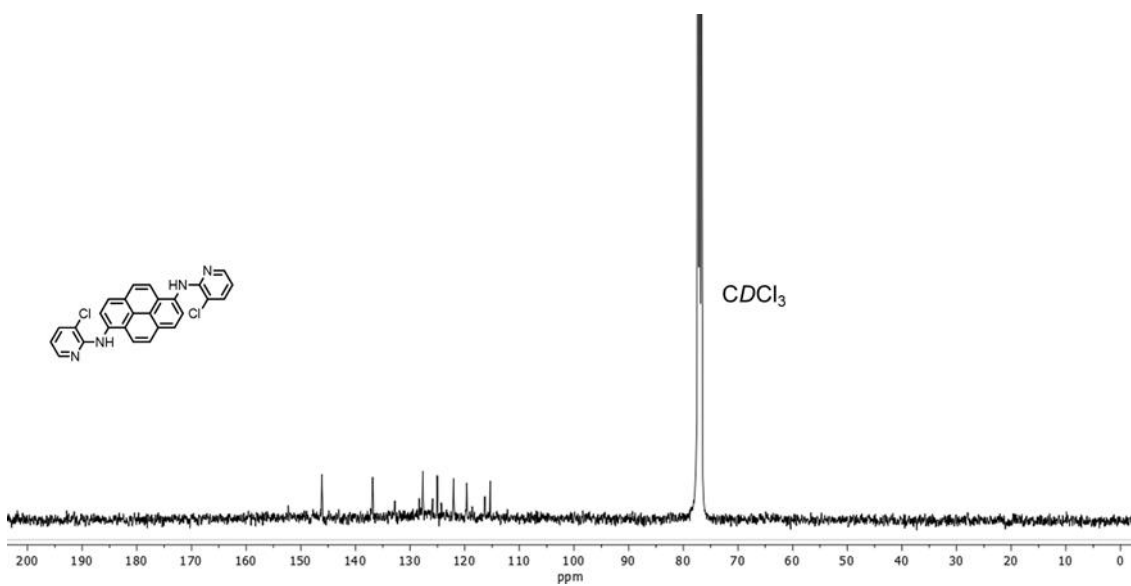
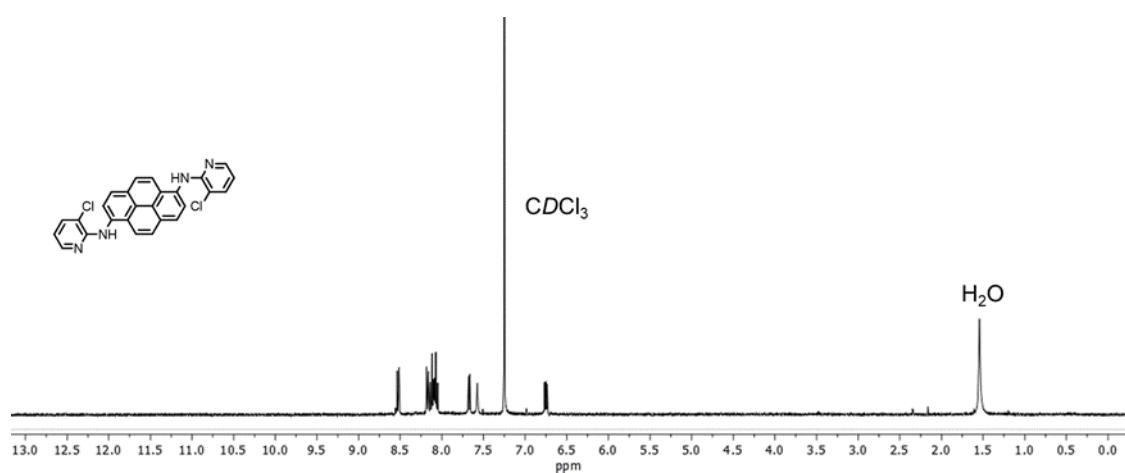


Fig. S3 ¹H-NMR and ¹³C-NMR spectra of compound **4** in CDCl₃.

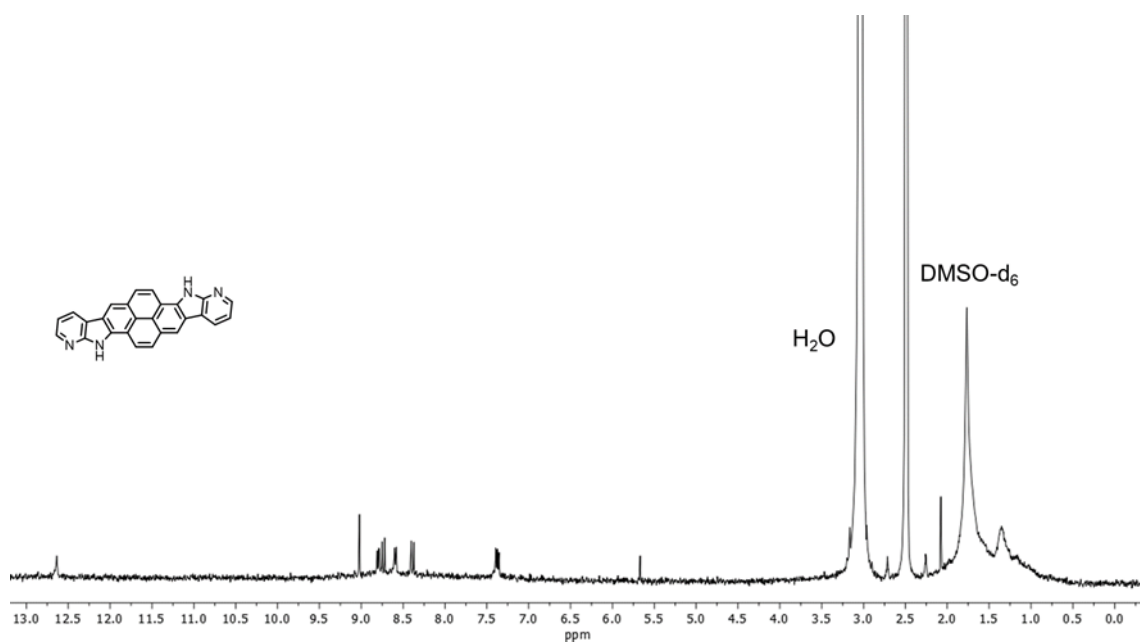


Fig. S4 ^1H -NMR spectrum of **PDAI** in DMSO-d_6 .

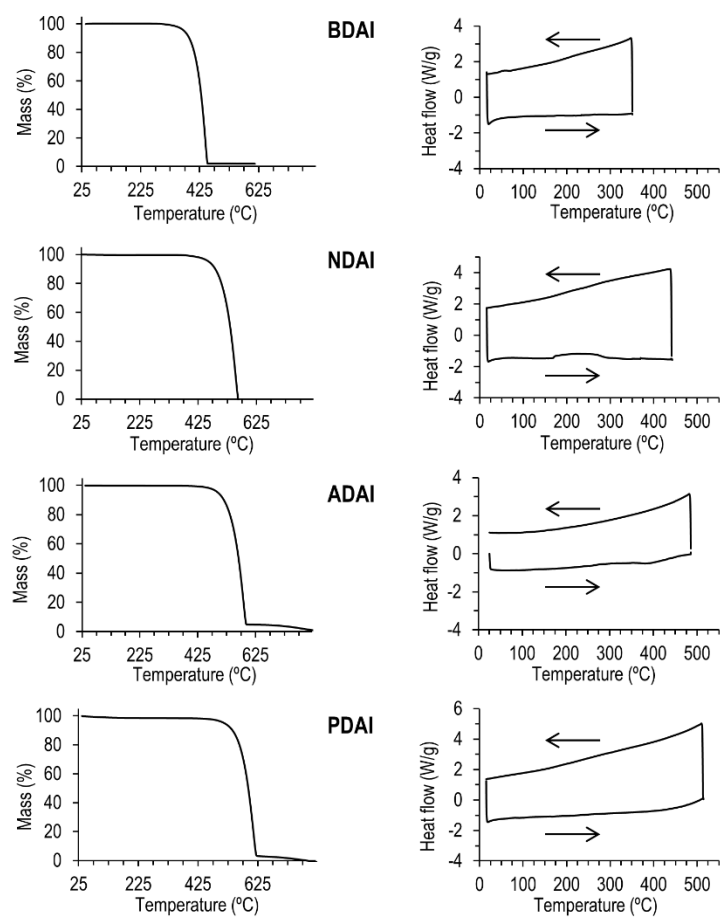


Fig. S5 Thermogravimetric analysis (TGA, left) and differential scanning calorimetry (DSC, right).

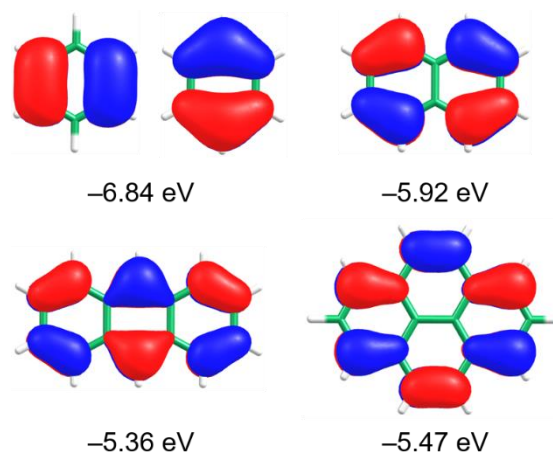


Fig. S6 Isocontours (± 0.03) and energies calculated for the highest-occupied molecular orbital (HOMO) of benzene, naphthalene, anthracene and pyrene at the B3LYP/6-31G** level in DMF as solvent.

Table S1 Low-lying singlet excited states (S_n) calculated at the TD-DFT B3LYP/6-31G** level using DMF as solvent for **BDAI**, **NDAI**, **ADAI** and **PDAI**. Vertical excitation energies (E), oscillator strengths (f) and dominant monoexcitations with contributions (within parentheses) greater than 20%.

	State	E (eV/nm)	f	Monoexcitations (%) ^a
BDAI	S_1	3.28 / 378	0.046	H→L (96)
	S_2	3.77 / 329	0.751	H-1→L (92)
	S_3	4.22 / 293	0.000	H→L+1 (93)
	S_4	4.43 / 280	0.000	H-2→L (91)
	S_5	4.65 / 267	1.201	H→L+2(90)
NDAI	S_1	3.39 / 366	0.206	H→L (89)
	S_2	3.76 / 330	0.290	H-1→L (64)
	S_3	4.11 / 301	0.000	H→L+1 (30)
	S_4	4.14 / 299	1.490	H→L+2 (82)
	S_5	4.30 / 288	0.000	H-1→L (64) H-1→L (31) H-2→L (76)
ADAI	S_1	2.93 / 423	0.088	H→L (97)
	S_2	3.27 / 379	0.071	H→L+1 (69)
	S_3	3.75 / 331	2.345	H-1→L (28) H-1→L (69) H→L+1 (28)
	S_4	3.76 / 330	0.000	H-2→L (89)
	S_5	4.82 / 295	0.000	H→L+2 (85)
PDAI	S_1	2.82 / 439	0.173	H→L (85)
	S_2	3.23 / 384	0.239	H→L+1 (70) H-1→L (20)
	S_3	3.54 / 351	0.000	H→L+2 (95)
	S_4	3.71 / 334	1.755	H-1→L (74) H→L+1 (21)
	S_5	3.97 / 312	0.000	H→L+2 (62) H-2→L (33)

^a H and L denote HOMO and LUMO, respectively.

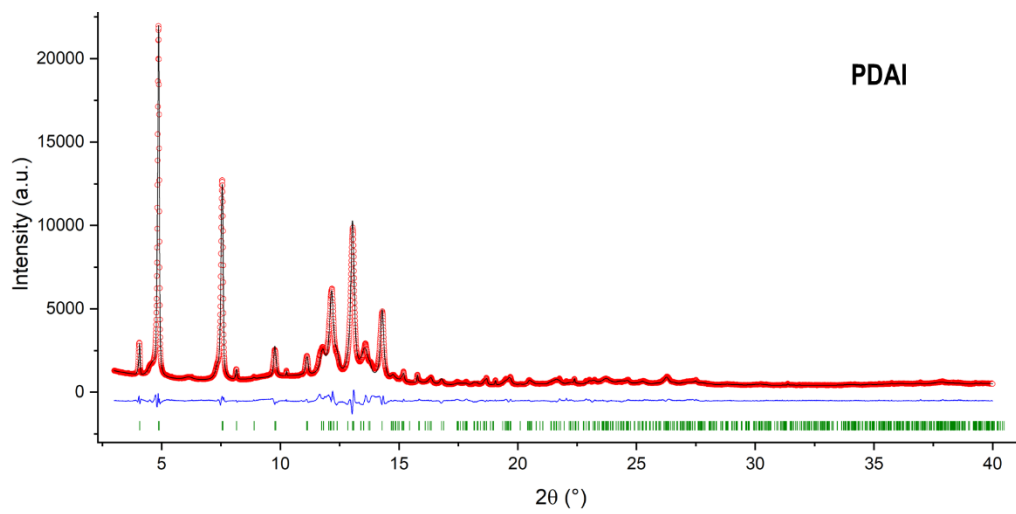
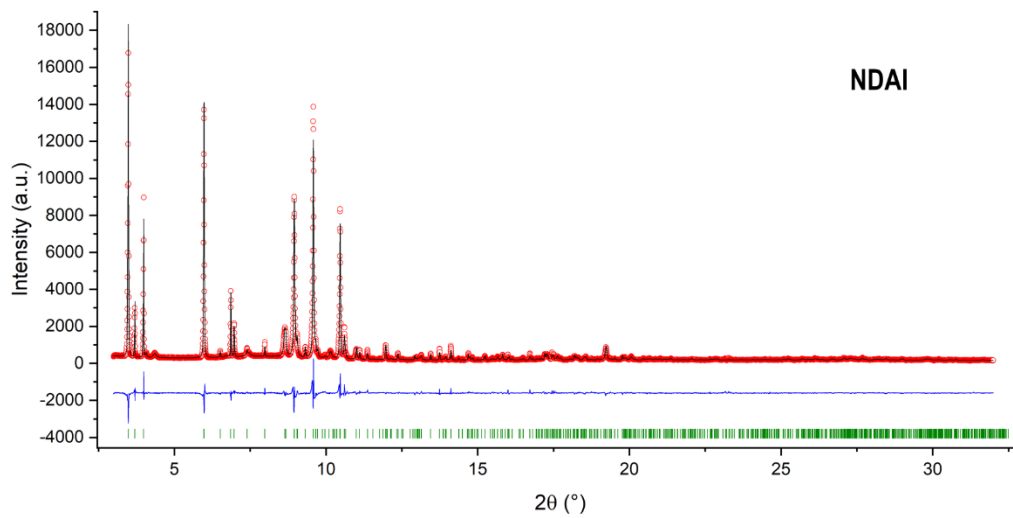
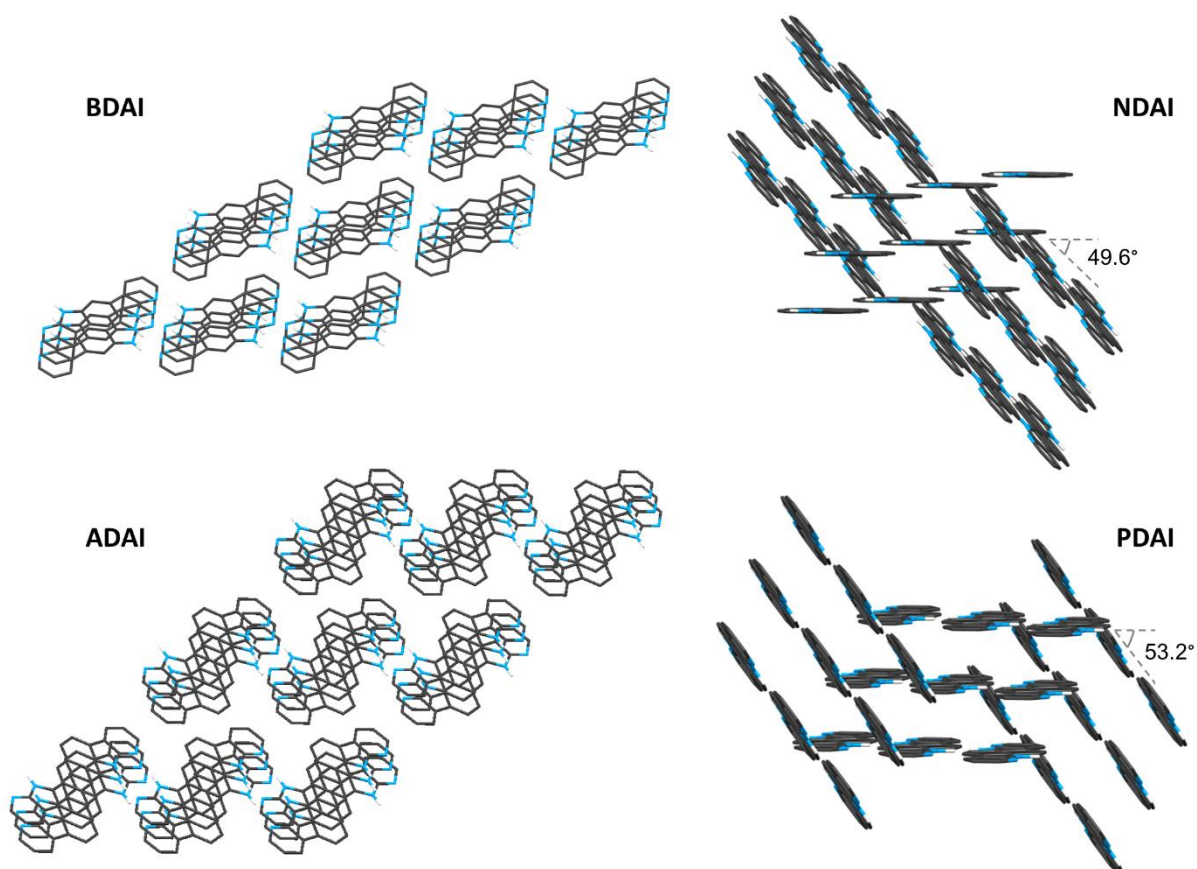


Fig. S7 Rietveld refinement plots for **NDAI** and **PDAI**, showing the experimental (red circles), calculated (black line) and difference profiles (blue line); green marks indicate reflection positions.

Table S2 Crystallographic data and Rietveld refinement summary for **NDAI** and **PDAI**.

Compound	NDAI	PDAI
Formula	C ₂₀ H ₁₂ N ₄	C ₂₆ H ₁₄ N ₄
Formula weight (g/mol)	308.34	382.42
Crystal system	Monoclinic	Monoclinic
Space group	<i>C</i> 2/ <i>c</i>	<i>C</i> 2/ <i>c</i>
<i>a</i> (Å)	18.9803(3)	23.9137(16)
<i>b</i> (Å)	3.84164(4)	3.84586(15)
<i>c</i> (Å)	20.1533(5)	19.9844(19)
<i>b</i> (°)	112.6085(10)	114.399(4)
<i>V</i> (Å ³)	1356.56(4)	1673.8(2)
<i>Z</i>	4	4
Radiation type	Synchrotron	Synchrotron
Diffractometer	SpLine (BM25A) at the ESRF, Grenoble	SpLine (BM25A) at the ESRF, Grenoble
Data collection mode	Transmission	Transmission
Wavelength (Å)	0.56523	0.77449
<i>R_p</i> (%)	6.48	4.03
<i>R_{wp}</i> (%)	8.46	5.35
<i>R_{exp}</i> (%)	5.19	3.21
<i>R_B</i> (%)	4.20	1.92
<i>Goodness-of-fit</i>	1.63	1.66

**Fig. S8** Expanded crystal packing for **BDAI**, **NDAI**, **ADAI** and **PDAI**.

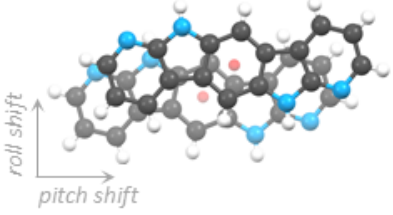
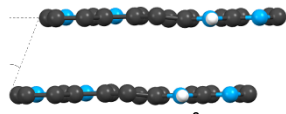
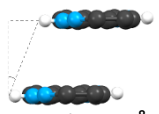

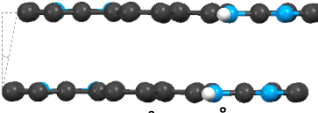
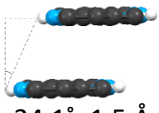
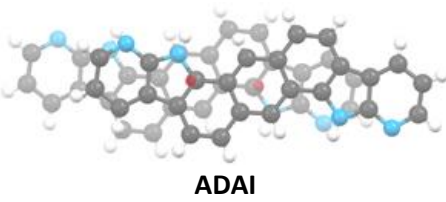
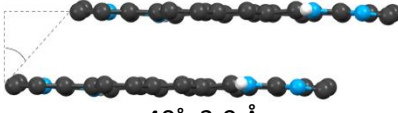
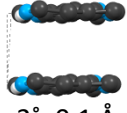
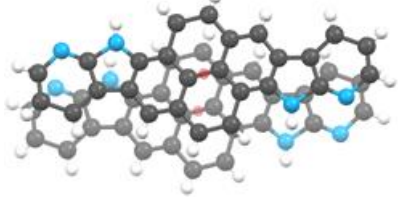
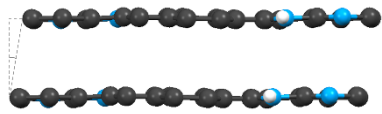
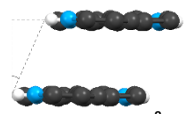
Top view of π -stacking	Pitch angle; Pitch shift	Roll angle; Roll shift
 <p>BDAI</p>	 <p>21°; 1.4 Å</p>	 <p>21.6°; 1.5 Å</p>
 <p>NDAI</p>	 <p>10.8°; 0.7 Å</p>	 <p>24.1°; 1.5 Å</p>
 <p>ADAI</p>	 <p>40°; 3.0 Å</p>	 <p>2°; 0.1 Å</p>
 <p>PDAI</p>	 <p>9.4°; 0.6 Å</p>	 <p>23.6°; 1.5 Å</p>

Fig. S9 Pitch and roll angles and shifts between adjacent π -stacked molecules.

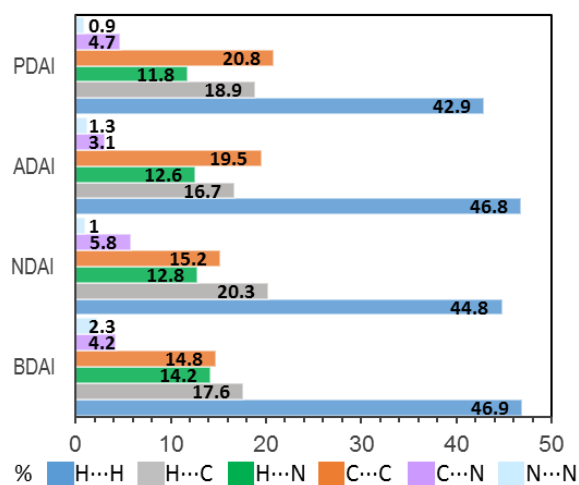


Fig. S10 Representative percentage contribution of the different non-covalent interactions (atom-to-atom) around the Hirshfeld surface.

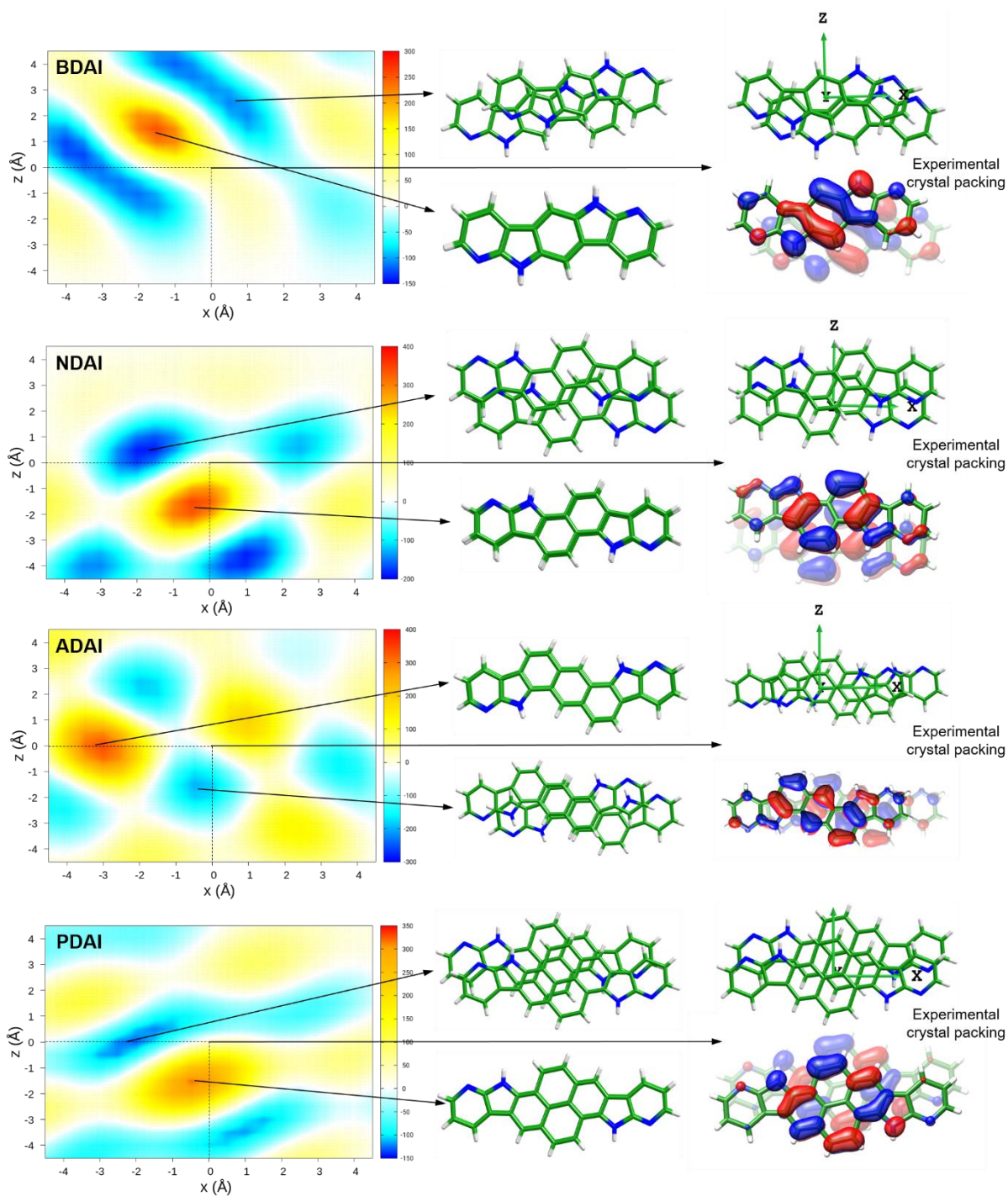
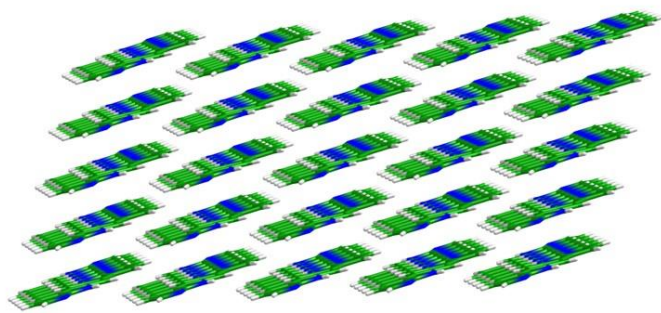
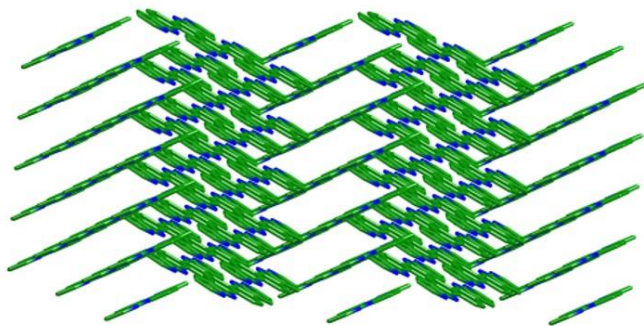
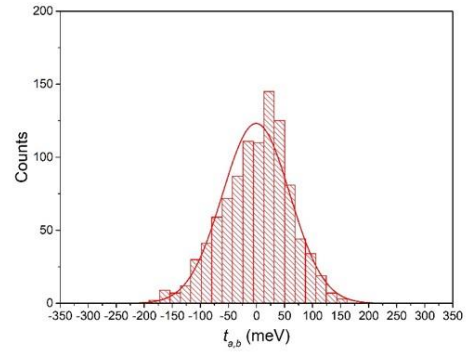


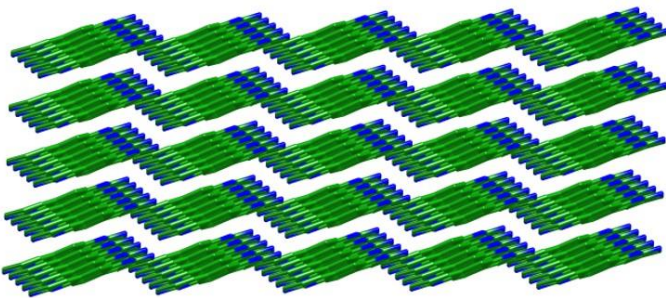
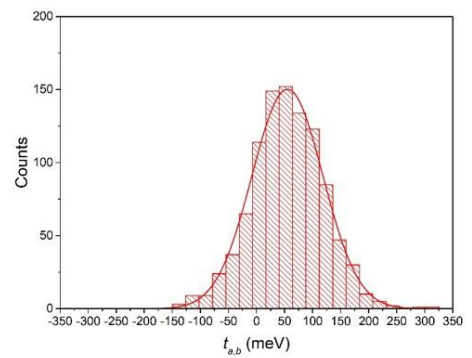
Fig. S11 2D maps of the $t_{1,2} = t_{1,3}$ transfer integral (in meV) for face-to-face π -stacked dimers of **BDAI**, **NDAI**, **ADAI** and **PDAI** calculated by moving one of the molecules along the x and z directions starting from the crystal structure ($x = 0 \text{ \AA}$ and $z = 0 \text{ \AA}$). The topologies of the superposed HOMOs are shown for the π -stacked dimers at the crystal structure (top and bottom molecules are represented with bright and faded colors, respectively).



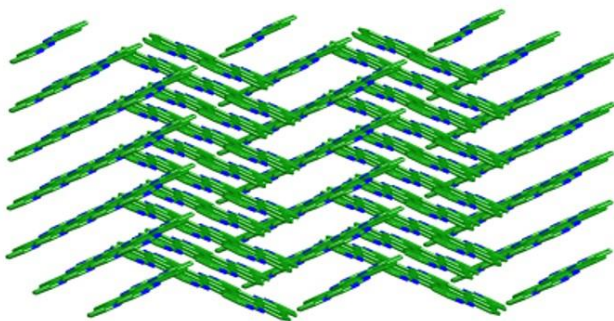
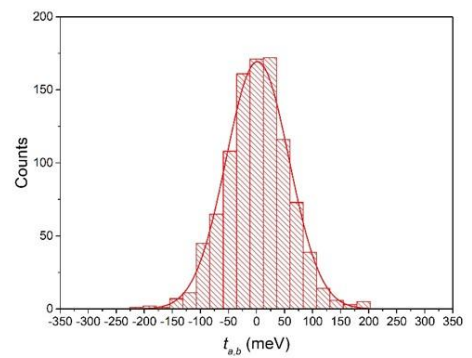
BDAI



NDAI



ADAI



PDAI

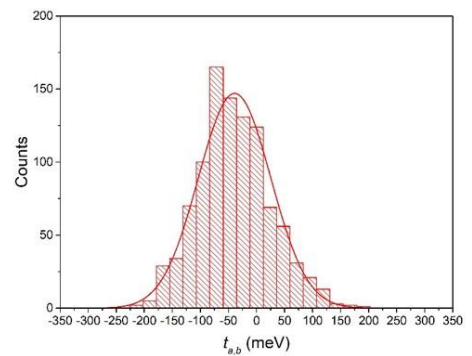


Fig. S12 Representation of the $5 \times 5 \times 5$ crystal slabs used in the MD simulation (left) and distributions of the values calculated for the $t_{1,2} = t_{1,3}$ transfer integral along the MD simulation (right).

Table S3 Average hole transfer integrals ($\langle t \rangle$), their fluctuations (σ_t), average squared transfer integrals ($\langle t^2 \rangle$), reorganisation energies (λ) and hole-transfer rate constants (k) estimated for the most relevant dimers of **BDAI**, **NDAI**, **ADAI** and **PDAI**.

Dimer ^a		BDAI	NDAI	ADAI	PDAI
	λ (meV)	233	250	182	239
1-2 = 1-3	$\langle t \rangle$ (meV)	-0.7	55.1	0.0	-39.1
	σ_t (meV)	60.1	63.2	57.8	64.6
	$\langle t^2 \rangle$ (meV ²)	3612.5	7030.3	3340.8	5702.0
	k (s ⁻¹)	1.3×10^{13}	2.1×10^{13}	2.2×10^{13}	1.9×10^{13}
1-4 = 1-5	$\langle t \rangle$ (meV)	-7.4	6.8	3.2	3.9
	σ_t (meV)	5.7	3.1	2.6	2.2
	$\langle t^2 \rangle$ (meV ²)	87.3	55.9	17.0	20.1
	k (s ⁻¹)	3.1×10^{11}	1.6×10^{11}	1.1×10^{11}	7.6×10^{10}
1-6 = 1-7	$\langle t \rangle$ (meV)	3.8	12.1	17.2	6.7
	σ_t (meV)	4.3	6.7	7.8	4.3
	$\langle t^2 \rangle$ (meV ²)	32.9	191.3	356.7	63.4
	k (s ⁻¹)	1.2×10^{11}	5.6×10^{11}	2.4×10^{12}	2.1×10^{11}
1-8 = 1-9	$\langle t \rangle$ (meV)	-23.9	2.2	-12.4	-0.5
	σ_t (meV)	13.9	3.7	6.4	4.6
	$\langle t^2 \rangle$ (meV ²)	764.4	18.5	194.7	21.4
	k (s ⁻¹)	2.7×10^{12}	5.5×10^{10}	1.3×10^{12}	7.2×10^{10}

^a See Fig. 4 in the main text for molecular numbering.

The data in Table S3 displays the average transfer integral ($\langle t \rangle$), its fluctuation (σ_t) and the average squared transfer integrals ($\langle t^2 \rangle$), obtained from the analysis of the dynamical disorder, together with the reorganisation energy and the rate constants computed for the most relevant dimers (1-2 = 1-3, 1-4 = 1-5, 1-6 = 1-7 and 1-8 = 1-9). The analysis of the data reveal that large fluctuations are only obtained for the π -stacked dimers (1-2 = 1-3). This is an expected result because relative displacements are less hindered for this dimer. The computed σ_t values are indeed higher than the $\langle t \rangle$ values, and the fluctuations in these dimers are the key factor determining the high values of $\langle t^2 \rangle$ for all the compounds. Nevertheless, it is necessary to perform a global analysis of the different $\langle t^2 \rangle$ contributions, along with the effect of the reorganisation energy, to get a general perception of the different charge hopping pathways influencing the charge transport process. Accordingly, H-bonded dimers (1-4 = 1-5), dimers diagonally interacting between parallel stacked ribbons (1-6 = 1-7) and dimers interacting between adjacent non-stacked ribbons (1-8 = 1-9) were also considered in addition to π -stacked dimers (1-2 = 1-3). These couplings show that alternative charge carrier pathways become significant, particularly in the case of 1-6 = 1-7 dimers, setting differences between the series of hydrogen-bonded molecules that result in a better performance of **ADAI** as organic semiconductor.

References

1. C. Lee, W. Yang and R. G. Parr, *Phys. Rev. B*, 1988, **37**, 785-789.
2. A. D. Becke, *Phys. Rev. A*, 1988, **38**, 3098-3100.
3. M. M. Francl, W. J. Pietro, W. J. Hehre, J. S. Binkley, M. S. Gordon, D. J. DeFrees and J. A. Pople, *J. Chem. Phys.*, 1982, **77**, 3654-3665.
4. S. Grimme, J. Antony, S. Ehrlich and H. Krieg, *J. Chem. Phys.*, 2010, **132**, 154104.
5. S. Grimme, S. Ehrlich and L. Goerigk, *J. Comput. Chem.*, 2011, **32**, 1456-1465.
6. A. D. Becke and E. R. Johnson, *J. Chem. Phys.*, 2005, **123**, 154101.
7. Gaussian 16, Revision A.03, M. J. Frisch, G. W. Trucks, H. B. Schlegel, G. E. Scuseria, M. A. Robb, J. R. Cheeseman, G. Scalmani, V. Barone, G. A. Petersson, H. Nakatsuji, X. Li, M. Caricato, A. V. Marenich,

- J. Bloino, B. G. Janesko, R. Gomperts, B. Mennucci, H. P. Hratchian, J. V. Ortiz, A. F. Izmaylov, J. L. Sonnenberg, D. Williams-Young, F. Ding, F. Lipparini, F. Egidi, J. Goings, B. Peng, A. Petrone, T. Henderson, D. Ranasinghe, V. G. Zakrzewski, J. Gao, N. Rega, G. Zheng, W. Liang, M. Hada, M. Ehara, K. Toyota, R. Fukuda, J. Hasegawa, M. Ishida, T. Nakajima, Y. Honda, O. Kitao, H. Nakai, T. Vreven, K. Throssell, J. A. Montgomery, Jr., J. E. Peralta, F. Ogliaro, M. J. Bearpark, J. J. Heyd, E. N. Brothers, K. N. Kudin, V. N. Staroverov, T. A. Keith, R. Kobayashi, J. Normand, K. Raghavachari, A. P. Rendell, J. C. Burant, S. S. Iyengar, J. Tomasi, M. Cossi, J. M. Millam, M. Klene, C. Adamo, R. Cammi, J. W. Ochterski, R. L. Martin, K. Morokuma, O. Farkas, J. B. Foresman, and D. J. Fox, Gaussian, Inc., Wallingford CT, 2016.
8. G. Scalmani and M. J. Frisch, *J. Chem. Phys.*, 2010, **132**, 114110.
 9. Chemcraft - graphical software for visualization of quantum chemistry computations. <https://www.chemcraftprog.com>
 10. C. Adamo and D. Jacquemin, *Chem. Soc. Rev.*, 2013, **42**, 845-856.
 11. M. E. Casida, C. Jamorski, K. C. Casida and D. R. Salahub, *J. Chem. Phys.*, 1998, **108**, 4439-4449.
 12. B. Baumeier, J. Kirkpatrick and D. Andrienko, *Phys. Chem. Chem. Phys.*, 2010, **12**, 11103-11113.
 13. C. Bannwarth, S. Ehlert and S. Grimme, *J. Chem. Theory Comput.*, 2019, **15**, 1652-1671.
 14. V. Coropceanu, J. Cornil, D. A. da Silva Filho, Y. Olivier, R. Silbey and J.-L. Brédas, *Chem. Rev.*, 2007, **107**, 926-952.